Title
Iterative Blade Element Momentum Theory for a Coaxial Rotor

Journal
Proceedings of the Vertical Flight Society 75th Annual Forum and Technology Display

Authors
Lee, Seongkyu
Dassonville, Maxime

Publication Date
2019-05-13

DOI
10.4050/f-0075-2019-14510

Iterative Blade Element Momentum Theory for a Coaxial Rotor

Seongkyu Lee Assistant Professor
Maxime Dassonville Undergraduate Student
Department of Mechanical and Aerospace Engineering
University of California, Davis
Davis, California, 95616 U.S.A.

ABSTRACT

This paper presents a new blade element momentum theory (BEMT) for a coaxial rotor in hover. The new BEMT solves the upper and lower rotor induced velocities iteratively so that the mutual rotor-to-rotor interaction is accounted for. The upper rotor induced velocity is affected by the lower rotor thrust and induced velocity, while the lower rotor induced velocity is affected by the upper rotor thrust and induced velocity. Two empirical constants are included in each rotor calculation. This new BEMT provides the performance of each rotor as a function of the rotor separation distance. The new BEMT is validated with measurement data for two coaxial rotor experiments. The first experiment validates the thrust to power coefficients at a given separation distance. The second experiment validates each rotor's figure of merit, thrust, power, interference loss factors, etc., as a function of the rotor separation distance. It is shown that the BEMT captures the trends and magnitudes of the performance as a function of the rotor separation distance compared to the measurement data. Detailed radial distributions of aerodynamic properties are also presented at several separation distances.

INTRODUCTION

A coaxial rotor has distinctive advantages over a single rotor. A counter-rotating rotor cancels out the yaw moment generated by each rotor so that the torque balance is met without a tail rotor. A removal of tail rotor enables the design of the vehicle system to be simpler and provides additional space in the tail. Auxiliary propellers can often be installed in the tail of the coaxial rotorcraft, which provides an additional propulsive force and enables a high-speed flight of rotorcraft (Ref. 1).

Recently, a lift-offset coaxial rotor has gained a renewed interest in military rotorcraft operation. A lift-offset coaxial rotor is designed to provide additional lift on the advancing side of each rotor (Refs. 2,3). This concept provides higher lift on the advancing side and lower lift on the retreating side. A reduced angle of attack on the retreating side helps mitigate dynamic stall and, hence, allows the rotorcraft to fly at a much faster speed compared to conventional helicopters without the issues due to dynamic stall. Numerical studies on a lift-offset coaxial rotor can be found from references (Refs. 4–8).

Ramasamy (Ref. 9) investigated the performance of a model-scaled coaxial rotor for untwisted and twisted rotor blades. He presented the effect of axial separation distance on the rotor performance such as the thrust, torque, and figure of merit. This experimental research provides benchmark cases for the validation of numerical studies of a coaxial rotor in hover (Ref. 10). Bhagwat (Ref. 11) analyzed the comparison between a co-rotating coaxial rotor with a counter-rotating coaxial rotor. He found that the swirl loss and recovery play a small role in the performance of coaxial rotor.

The blade element momentum theory (BEMT) is one of the simplest numerical methods to analyze rotorcraft aerodynamics and performance in hover and axial flights. The BEMT has been well validated for rotorcraft performance (Ref. 12), and it has been widely used as a preliminary design tool in rotorcraft industry.

Payne (Ref. 13) first considered the momentum theory for a coaxial rotor. He assumed that two rotors are positioned on the same rotor disk and each rotor generates the half of the total thrust. This approach resulted in significant overpredictions of rotor induced power since the method did not consider the axial finite separation distance between two rotors. Leishman (Ref. 14) proposed a new BEMT approach for a coaxial rotor. The model accounts for the separation distance between two rotors and the influence from the upper rotor on the lower rotor. The induced inflow on the lower rotor disk is adjusted with the inflow of the upper rotor wake within the boundary in which the upper rotor tip vortex contraction meets on the lower rotor disk plane. The two main assumptions that Leishman used are 1) the contracted wake area of the upper rotor is known such as the ideal case in which the distance between the upper rotor and the lower rotor is infinite and 2) the influence from the lower rotor on the upper rotor is neglected. Although these two assumptions make the analysis simpler, they do not properly represent a realistic coaxial rotor system. In particular, the rotor separation distance is relatively short for most coaxial rotors, so the effect of the separation dis-

Presented at the Vertical Flight Society 75th Annual Forum & Technology Display, Philadelphia, Pennsylvania, May 13–16, 2019.

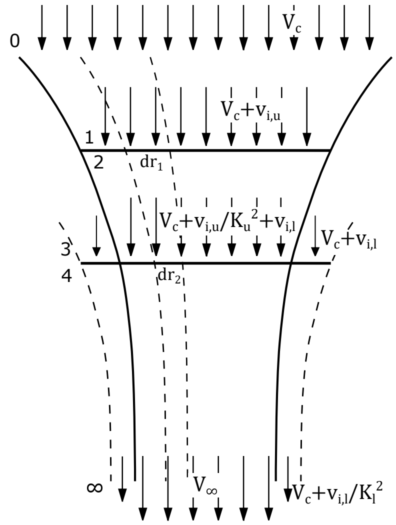

Fig. 1. Wake contraction for a coaxial rotor.

tance should be considered in the rotor wake contraction and the effect of the lower rotor on the upper rotor cannot be ignored as shown in Ramasamy's experimental study (Ref. 9). Giovanetti and Hall (Ref. 15) included the influence of the lower rotor on the upper rotor using the Bio-Savart law and an empirical parameter. However, they assumed a uniform axial inflow acting on the upper rotor that is induced by the lower rotor. They approximated the upper rotor wake contraction as a function of vertical separation using this Biot-Savart law and the empirical constant. However, this equation provides the induced velocity measured at $r = 0$, which does not vary radially.

In the current paper, we propose a new BEMT for a coaxial rotor. We remove the assumptions that were used in earlier models. We account for the actual finite axial separation distance in a coaxial rotor, include the mutual interaction between the upper rotor and the lower rotor, and handle a non-uniform induced velocity. This new BEMT provides predictions of coaxial rotor performance as a function of axial separation distance. The new BEMT code is validated with two experiments, especially for the aerodynamic performance as a function of the separation distance of a coaxial rotor in hover.

ITERATIVE BLADE ELEMENT MOMENTUM THEORY

In this section, an iterative BEMT approach that solves the upper and lower rotors simultaneously will be derived. The upper rotor solution includes the influence of the lower rotor and the lower rotor solution includes the influence of the upper rotor. The axial separation distance plays an important role in the rotor-to-rotor interaction. The BEMT is iterated until the performance of each rotor is converged. Two trim conditions are applied: torque balance and required thrust.

Figure 1 shows the control volume with two rotors. The climb velocity, V_c, is included for axial flight. For hover, V_c is zero. The Bernoulli equations can be written in each section:

$$P_0 + \frac{1}{2}\rho V_c^2 = P_1 + \frac{1}{2}\rho V_1^2 \tag{1}$$

$$P_2 + \frac{1}{2}\rho V_2^2 = P_3 + \frac{1}{2}\rho V_3^2 \tag{2}$$

$$P_4 + \frac{1}{2}\rho V_4^2 = P_\infty + \frac{1}{2}\rho V_\infty^2 \tag{3}$$

Note that $V_1 = V_2$, $V_3 = V_4$, and $P_0 = P_\infty$.

The sectional thrust in the streamtube for the upper rotor is written as

$$\frac{dT_1}{dA_1} = P_2 - P_1 = P_3 - P_0 + \frac{1}{2}\rho V_3^2 - \frac{1}{2}\rho V_c^2 \tag{4}$$

Using the following equation

$$P_3 = P_4 - \frac{dT_2}{dA_2} = P_\infty + \frac{1}{2}\rho V_\infty^2 - \frac{1}{2}\rho V_4^2 - \frac{dT_2}{dA_2} \tag{5}$$

the sectional thrust becomes

$$\frac{dT_1}{dA_1} = -\frac{dT_2}{dA_2} + \frac{1}{2}\rho V_\infty^2 - \frac{1}{2}\rho V_c^2 \tag{6}$$

or

$$dT_1 = dA_1 \left[-\frac{dT_2}{dA_2} + \frac{1}{2}\rho V_\infty^2 - \frac{1}{2}\rho V_c^2 \right] \tag{7}$$

Finally, we can find that

$$\frac{dT_1}{dA_1} + \frac{dT_2}{dA_2} = \frac{\rho}{2}\left[V_\infty^2 - V_c^2\right] \tag{8}$$

Equation (8) simply represents that the change in the dynamic pressure between the outlet and inlet is equivalent to the total force per unit area acting on the streamtube from two rotors.

Let us define y as the radial distance of a streamtube at the tip and that $K_t = y_\infty/y_1$ is the contraction ratio from 1 to ∞ in the presence of the lower rotor, $K_u = y_3/y_1$ is the contraction ratio from the upper rotor to the lower rotor, and $K_l = y_\infty/y_3$ is the contraction ratio from 3 to ∞.

The far downstream velocity within the slipstream of the upper rotor becomes

$$V_\infty = V_c + \frac{v_{i,u}}{K_t^2} + \frac{v_{i,l}}{K_l^2} \tag{9}$$

where $v_{i,u}$ and $v_{i,l}$ are the induced velocities by the upper and lower rotors at each rotor plane, as shown in Fig 1. Outside the slipstream of the upper rotor, $v_{i,u}$ becomes zero.

Then, Eq. (8) becomes

$$\frac{dT_u}{dA_u} + \frac{dT_l}{dA_l} = \frac{\rho}{2}\left[\left(V_c + \frac{v_{i,u}}{K_t^2} + \frac{v_{i,l}}{K_l^2}\right)^2 - V_c^2\right] \tag{10}$$

or

$$\frac{dC_{T_u}}{2\pi y_u dy_u} + \frac{dC_{T_l}}{2\pi y_l dy_l K_u^2} = \frac{\rho}{2\rho(\pi R^2)(\Omega R)^2}\left[\left(V_c + \frac{v_{i,u}}{K_t^2} + \frac{v_{i,l}}{K_l^2}\right)^2 - V_c^2\right] \tag{11}$$

Rearranging the above equation yields

$$V_c^2 + \frac{\Omega^2 R^4}{y_u dy_u}\left(dC_{T_u} + \frac{dC_{T_l}}{K_u^2}\right) = \left(V_c + \frac{v_{i,u}}{K_t^2} + \frac{v_{i,l}}{K_l^2}\right)^2 \quad (12)$$

The solution for $v_{i,u}$ can be found as follows:

$$v_{i,u} = K_t^2\left[\sqrt{V_c^2 + \frac{\Omega^2 R^4}{y_u dy_u}\left(dC_{T_u} + \frac{dC_{T_l}}{K_u^2}\right)} - V_c - \frac{v_{i,l}}{K_l^2}\right] \quad (13)$$

or

$$v_{i,u} = K_t^2\sqrt{V_c^2 + \frac{\Omega^2 R^4}{y_u dy_u}\left(dC_{T_u} + \frac{dC_{T_l}}{K_u^2}\right)} - K_t^2 V_c - K_u^2 v_{i,l} \quad (14)$$

The non-dimensional induced velocity or inflow ratio for the upper rotor can be written as

$$\lambda_{i,u} = K_t^2\sqrt{\lambda_c^2 + \frac{1}{r_u dr_u}\left(dC_{T_u} + \frac{dC_{T_l}}{K_u^2}\right)} - K_t^2\lambda_c - K_u^2\lambda_{i,l} \quad (15)$$

where r represents the non-dimensionalized radial distance.

The non-dimensional induced velocity on the lower rotor can be similarly obtained as

$$\lambda_{i,l} = K_l^2\sqrt{\lambda_c^2 + \frac{1}{r_l dr_l}\left(K_u^2 dC_{T_u} + dC_{T_l}\right)} - K_l^2\lambda_c - \frac{\lambda_{i,u}}{K_u^2} \quad (16)$$

The total inflow ratios can be defined as

$$\lambda_u = \lambda_c + \lambda_{i,u}$$
$$\lambda_l = \begin{cases} \lambda_c + \lambda_{i,l} + \lambda_{i,u}/K_u^2 & \text{for} \quad r_l \le K_u r_{u,tip} \\ \lambda_c + \lambda_{i,l} & \text{for} \quad r_l > K_u r_{u,tip} \end{cases} \quad (17)$$

where $r_{u,tip}$ is the non-dimensionalized tip radius of the upper rotor.

Finally, adding the Prandtl's tip loss effect with the F function (Ref. 12) and two empirical constants, A and B, results in

$$\lambda_u = K_t^2\sqrt{\lambda_c^2 + \frac{1}{r_u dr_u}\left(\frac{dC_{T_u}}{F} + \frac{dC_{T_l}}{K_u^2}\right)} + (1-K_t^2)\lambda_c - K_u^2\lambda_{i,l} + A\lambda_{i,l} \quad (18)$$

and

$$\lambda_l = \begin{cases} K_l^2\sqrt{\lambda_c^2 + \frac{1}{r_l dr_l}\left(K_u^2 dC_{T_u} + \frac{dC_{T_l}}{F}\right)} + (1-K_l^2)\lambda_c - B\lambda_{i,u} \\ \text{for} \quad r_l \le K_u r_{u,tip} \\ K_l^2\sqrt{\lambda_c^2 + \frac{1}{r_l dr_l}\left(\frac{dC_{T_l}}{F}\right)} + (1-K_l^2)\lambda_c \\ \text{for} \quad r_l > K_u r_{u,tip} \end{cases} \quad (19)$$

Empirical constant, A, in Eq. (18) has been added to include the effect of the lower rotor on the upper rotor. This constant is multiplied by $\lambda_{i,l}$ so that the effect of the lower rotor depends on the magnitude of the induced velocity of the lower rotor. Since the induced velocity of the lower rotor varies as a function of the radial distance and the axial separation distance, the effect of the lower rotor on the upper rotor also varies with the rotor radial and axial separation distances. Empirical constant, B, in Eq. (19) has been added to augment the effect of the upper rotor on the lower rotor when the area is within the influence zone of the upper rotor wake. This empirical constant is multiplied by the induced velocity of the upper rotor. Since the induced velocity of the upper rotor is a function of the radial and separation distances, the effect of the upper rotor on the lower rotor is also a function of the radial and separation distances. It is found that A of 0.5 and B of 0.12 provide the closest agreement with the measurement data later.

Equations (18)–(19) can be solved by the BEMT for each rotor. However, it is worthwhile noting that the upper rotor inflow solution is influenced by the lower rotor thrust and lower rotor inflow in Eq. (18). Similarly, the lower rotor inflow is affected by the upper rotor thrust and upper rotor inflow in Eq. (19). Therefore, an iterative approach is required to solve these coupled equations. For example, for the upper rotor BEMT calculation, the lower rotor thrust and the lower rotor inflow ratio are known a priori from an earlier iteration or the initial assumption of zero for both. Then, the upper rotor BEMT determines the upper rotor thrust and the upper rotor inflow ratio. For the lower rotor BEMT calculation, the upper rotor thrust and the upper rotor inflow ratio are given from an earlier iteration or the initial assumption of zero for both. Then, the lower rotor BEMT determines the lower rotor thrust and the lower rotor inflow ratio. The rotor-to-rotor iteration is continued until the thrusts and the inflow ratios for both rotors are fully converged.

Since a streamtube contracts from the upper rotor to the lower rotor, the radial locations following the streamtube are not the same for both rotors. Furthermore, the influenced radial locations may not be on the designated control points, at which the aerodynamic data are defined. Therefore, a numerical interpolation is required on each rotor blade when coupling the upper rotor BEMT and lower rotor BEMT.

Prescribed wake contraction

The contraction ratio from the upper rotor to the lower rotor, K_u, depends on the axial separation distance. In order to include the effect of the axial separation distance, we use a prescribed wake contraction. Landgrebe (Ref. 16) proposed the prescribed wake model

$$\frac{z_{\text{tip}}}{R} = \begin{cases} k_1\psi_\omega & \text{for} \quad 0 \le \psi_\omega \le 2\pi/N_b \\ \left(\frac{z_{\text{tip}}}{R}\right)_{\psi_\omega = 2\pi/N_b} + k_2\left(\psi_\omega - \frac{2\pi}{N_b}\right) & \text{for} \quad \psi_\omega \ge 2\pi/N_b \end{cases} \quad (20)$$

$$\frac{y_{\text{tip}}}{R} = r_{\text{tip}} = A + (1-A)\exp(-\Lambda\psi_\omega) \quad (21)$$

where ψ_ω is the wake age, $k_1 = -0.25(C_T/\sigma + 0.001\theta_{tw})$, $k_2 = -(1.41 + 0.0141\theta_{tw})\sqrt{C_T/2}$, $A = 0.78$, and $\Lambda = 0.145 + 27C_T$. For our purpose, the wake age is determined from a fixed axial separation distance, z_{tip}, of interest from Eq. (20). From the determined wake age, the contracted radius, y_{tip}, is determined from Eq. (21). It should be noted that C_T is included in the parameter k_1 so that the wake contraction is a

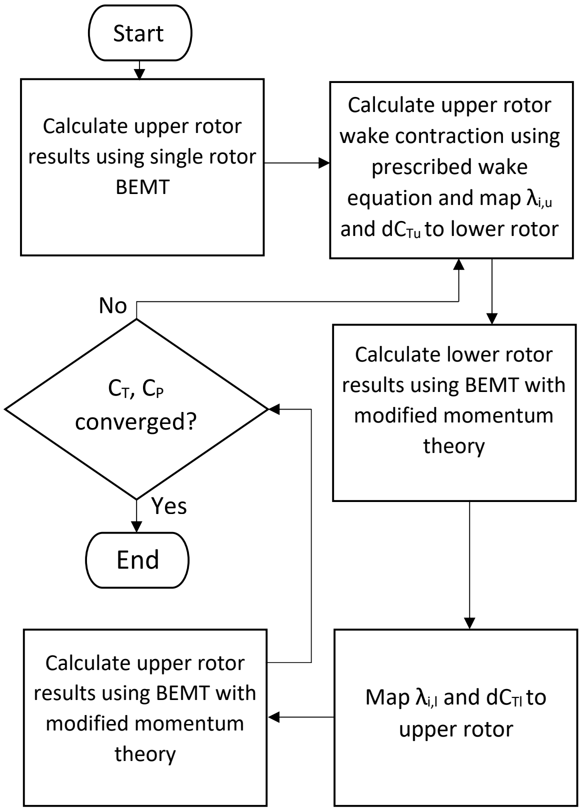

Fig. 2. Flow chart of the iterative BEMT method

function of the upper rotor thrust. Note that the upper thrust is also affected by the wake contraction in Eq. (18). Therefore, the computation of the prescribed wake contraction is fully included in the iterative BEMT process. This prescribed wake model provides the contraction ratio of 0.78 at the far downstream, which is larger than for the ideal case, which is 0.707, and consistent to the measured one. For this reason, we use K_l of 0.78 as well. However, K_t includes the double wake contraction effects: the wake contraction from the upper rotor to the lower rotor and then from the lower rotor to the far downstream so that $K_t = K_u \times K_l$. In this paper, we assume the same wake contraction from the root to the tip.

A flow chart of the iterative BEMT incorporating the prescribed wake is shown in Fig. 2.

Trim process

In the coaxial rotor, two trim conditions are considered. The first one is the balanced torque or $C_{Q_u} = C_{Q_l}$ where C_{Q_u} is the torque of the upper rotor and C_{Q_l} is the torque of the lower rotor. The second trim condition is the required total thrust or $C_{T_u} + C_{T_l} = C_{T_{\text{req}}}$ where C_{T_u} and C_{T_l} are the thrust of the upper and lower rotors, respectively, and $C_{T_{\text{req}}}$ is the required thrust. We use Broyden's Method to find the collective pitch angles (θ_u and θ_l) of the upper and lower rotors to meet these trim conditions.

The trim solution process is described as follows.

1. Let $\vec{\theta}^{(0)} = [\theta_u^{(0)}, \theta_l^{(0)}]$, $F_1(\theta_u, \theta_l) = C_{Q_u} - C_{Q_l}$, $F_2(\theta_u, \theta_l) = C_{T_u} + C_{T_l} - C_{T_{\text{req}}}$, and $\vec{F} = [F_1, F_2]$. The method finds the roots of $\vec{F}$.
2. Calculate $F_1(\vec{\theta}^{(0)})$ and $F_2(\vec{\theta}^{(0)})$ by solving the iterative BEMT.
3. Calculate $A_0^{-1} = J(\vec{\theta}^{(0)})^{-1}$, where J is the Jacobian matrix as follows:

$$\begin{bmatrix} \frac{\partial F_1(\vec{\theta}^{(0)})}{\partial \theta_u} & \frac{\partial F_1(\vec{\theta}^{(0)})}{\partial \theta_l} \\ \frac{\partial F_2(\vec{\theta}^{(0)})}{\partial \theta_u} & \frac{\partial F_2(\vec{\theta}^{(0)})}{\partial \theta_l} \end{bmatrix} \tag{22}$$

   The numerical differentiation is performed to find the Jacobian matrix.
4. Calculate $\vec{\theta}^{(1)} = \vec{\theta}^{(0)} - A_0^{-1} F(\vec{\theta}^{(0)})$.
5. Calculate the iterative BEMT to find $F(\vec{\theta}^{(1)})$.
6. Calculate $\vec{y}_1 = F(\vec{\theta}^{(1)}) - F(\vec{\theta}^{(0)})$.
7. Calculate $\vec{s}_1 = \vec{\theta}^{(1)} - \vec{\theta}^{(0)}$
8. Calculate $A_1^{-1} = A_0^{-1} + \frac{1}{\vec{s}_1^T A_0^{-1} \vec{y}_1} [(\vec{s}_1 - A_0^{-1} \vec{y}_1) \vec{s}_1^T A_0^{-1}]$.
9. Calculate $\vec{\theta}^{(2)} = \vec{\theta}^{(1)} - A_1^{-1} F(\vec{\theta}^{(1)})$.
10. Repeat steps 4-9 until the L2 norm error is below the convergence criteria. The resulting θ_u and θ_l are in torque-balanced condition.

Figure 3 shows a flowchart of the overall numerical process, which includes the iterative BEMT, torque balance, and sweep of the separation distance. The *iterative BEMT* in the flow chart indicates the flow chart shown in Fig. 2.

RESULTS

In this section, a standard single rotor BEMT is first validated for an isolated rotor to find the lift slope and drag polar coefficients for a selected rotor, and then the proposed iterative BEMT is validated against the measurement data of the coaxial rotor performance (Refs. 9, 17). In particular, the effect of the axial separation distance on the upper rotor, lower rotor, and coaxial rotor performance is predicted by the BEMT for the first time. An untwisted rotor blade and two thrust conditions are considered for these detailed analyses. The separation loss, interference loss, and rotor-to-rotor influence loss in a coaxial system are also studied in comparison with a single rotor. The local distributions of the thrust, inflow, and angle of attack are analyzed at different axial distances for two thrust cases.

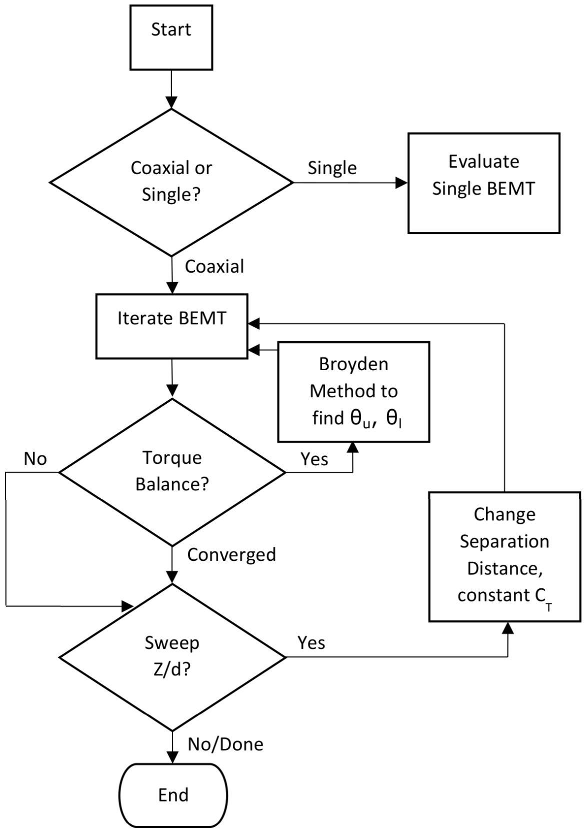

Fig. 3. Flow chart of the method

Validation Case 1

In this subsection, the iterative BEMT predictions are validated with experimental data of Harrington's two rotor cases (Ref. 17). The rotor has two blades and the rotor radius is 12.5 ft. For rotor 1, the rotor blade is tapered with a taper ratio of 0.39 and, for rotor 2, the blade is not tapered. The rotor-to-rotor separation distances for both rotors are 8% and 9.3% of the rotor diameter, respectively. The lift coefficient slope and the drag polar coefficients are obtained from the single rotor experiment validation, which is not shown here.

Figure 4 shows the thrust to power coefficients for the two rotor cases. The predictions are compared to the measured data for the single rotor and the coaxial rotor. It is shown that the predictions are in good agreement with the data for both cases. The coaxial rotor predictions are more accurate for rotor 2 (straight blade) than for rotor 1 (tapered blade). The upper and lower rotor predictions, which were obtained from the iterative BEMT for a coaxial rotor, are also included in the plot. For each rotor case, it is shown that the upper rotor generates more thrust than the lower rotor at the same power. In addition, the coaxial rotor generates more thrust than each individual rotor at the same power.

Figure 5 shows the figure of merit for both coaxial rotors. The traditional coaxial rotor figure of merit is calculated as follows (Ref. 18):

$$FM_{coax} = \frac{(C_{T,U} + C_{T,L})^{3/2}}{\sqrt{2}(C_{P,U} + C_{P,L})} \tag{23}$$

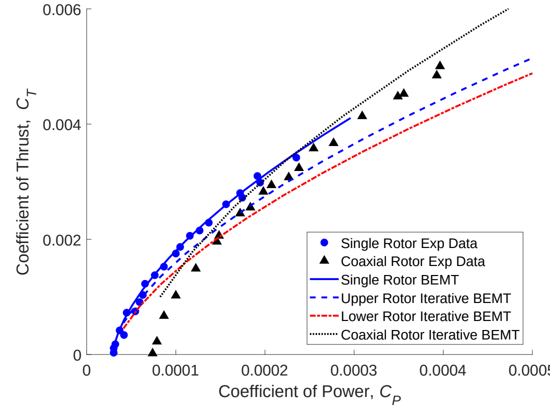

(a)

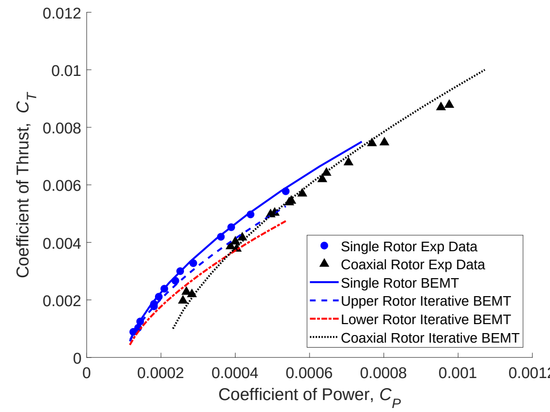

(b)

Fig. 4. Coaxial rotor BEMT validation for the power and thrust coefficients: (a) Harrington rotor 1 and (b) Harrington rotor 2.

where the subscripts, U and L, represent the upper rotor and the lower rotor, respectively. It is found that the single rotor BEMT accurately predicts the figure of merit of the single rotor. In coaxial rotor configurations, the predicted figure of merit for both the upper and lower rotors obtained by the iterative BEMT is lower than that of the single rotor. However, the upper rotor shows a higher figure of merit than the lower rotor. This is consistent with Fig. 4. The figure of merit for the coaxial rotor, as calculated in Eq. (23), shows good predictions compared to the measurement data. The prediction is slightly more accurate for Harrington rotor 2 (straight blade) than for Harrington rotor 1 (tapered blade), as shown in Fig. 5.

Validation Case 2

Although the Harrington's rotor cases were useful to validate the proposed iterative BEMT at a fixed separation distance, there were not enough data to predict the performance behaviors as a function of the axial separation distance. In this subsection, Ramasamy's coaxial rotor experimental data (Ref. 9) are used to validate the new iterative BEMT as a function of the axial separation distance. Ramasamy's experiment in-

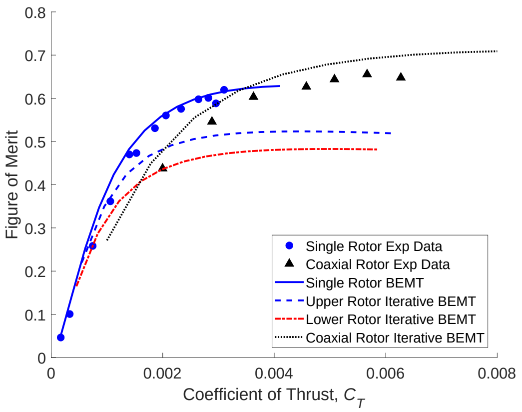

(a)

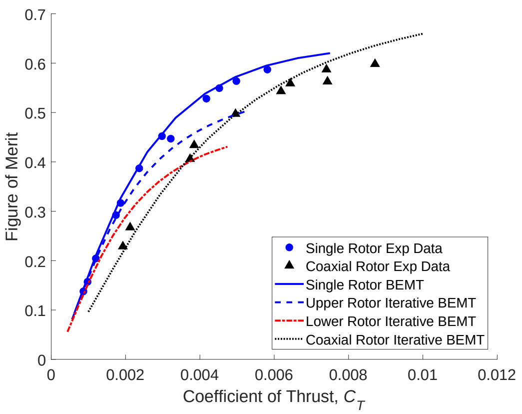

(b)

Fig. 5. Coaxial rotor BEMT validation for figure of merit: (a) Harrington rotor 1 and (b) Harrington rotor 2.

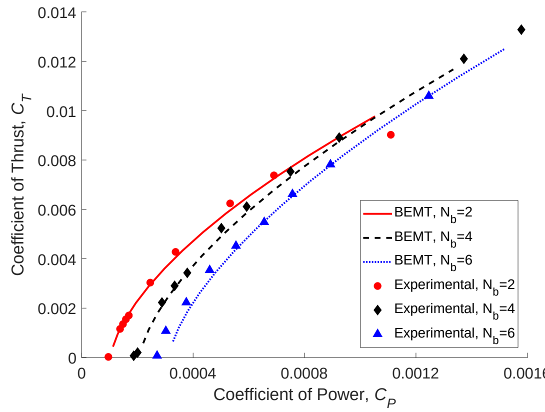

(a)

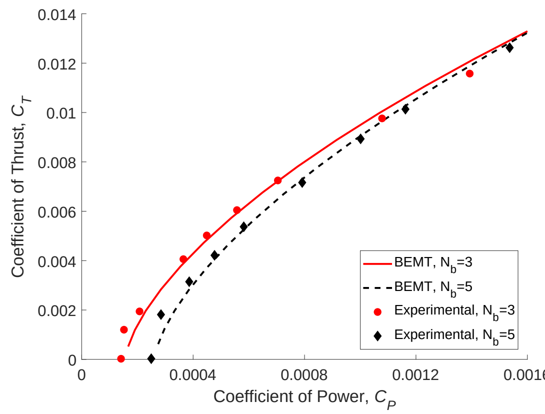

(b)

Fig. 6. Single rotor BEMT validation for the power and thrust coefficients: (a) the number of blades: 2, 4, 6 and (b) the number of blades: 3, 5.

cludes comprehensive and detailed performance results for a model-scaled coaxial rotor in hover.

The coaxial rotor of our choice for the validation has three blades on each rotor. The blade uses a NACA0012 untwisted airfoil. The blade radius is 2.17 ft and the chord length is 2.29 in. The root cutout is 19.1%. The rotor RPM is 800 and the tip Mach number is 0.25. The Reynolds number at the tip is 325,000.

Figures 6 and 7 show comparisons of BEMT predictions and measurement data for the power-thrust coefficients and the figure of merit for an isolated rotor with a various number of blades. In this validation study, we use the same definition of the modified figure of merit as Ramasamy used (Refs. 9, 19)

$$FM_{coax} = \frac{(C_{T,U}^{3/2} + C_{T,L}^{3/2})}{\sqrt{2}(C_{P,U} + C_{P,L})} \tag{24}$$

It is shown that the BEMT agrees very well with the measurement data, except for two blades at high thrust, in which the figure of merit decreases rapidly due to blade stall in the measurement while the prediction does not capture this stall behavior. This single rotor validation provides a slope of the lift coefficient and drag polar coefficients as a function of angle of attack, which are used for the coaxial rotor BEMT.

Figure 8 shows a convergence history of the thrust for the upper and lower rotors for two thrust values ($C_T = 0.007$ and 0.014) at two separation distances ($Z/d = 0.08$ and 1.0). The L2 norm of 1E-4 is used for the convergence criterion of the trim solution. The maximum errors of 7E-10 and 7E-11 are used for the convergence of C_T and C_P, respectively, for the iterative BEMT. In other words, the iterative BEMT is performed until both the error thresholds of C_T and C_P are met. In Fig. 8, the large peaks indicate the change of the trim solutions and small smooth transitions between the peaks indicate the convergence of the iterative BEMT. For a larger thrust value, the convergence takes more iterations than for a smaller thrust value. The trim solution is converged in about 5 iterations and the iterative BEMT is converged in about 10 iterations. For a smaller separation distance, the convergence takes more iterations than for a larger separation distance. For the number of iterations of 100 or 200, it only takes a couple of seconds on a desktop computer.

Figure 9 shows the wake contraction of the upper rotor up to the lower rotor, or K_u, which is calculated from Eqs (20)

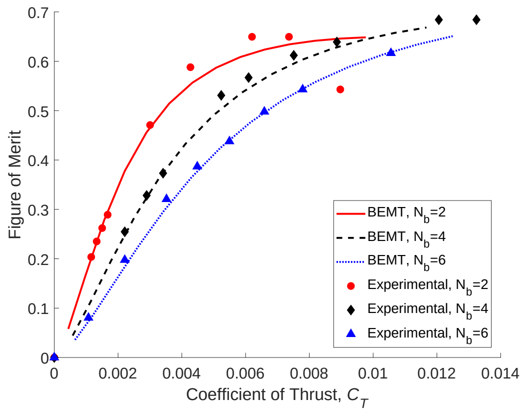

(a)

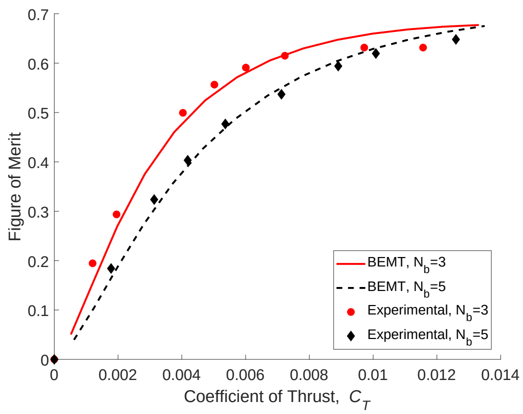

(b)

Fig. 7. Single rotor BEMT validation for figure of merit: (a) the number of blades: 2, 4, 6 and (b) the number of blades: 3, 5.

and (21). It is clearly visible that the upper rotor wake contraction varies with the rotor separation distance. At large distance, it is converged to 0.78 as expected. This contraction ratio determines the influence area in the lower rotor due to the upper rotor wake, and the value itself, K_u, is used in Eqs. (18) and (19) as well.

Figure 10 shows the effect of the axial separation distance on the figure of merit for the total coaxial thrust coefficient of 0.014. Both the prediction and the measurement data are included in the figure. It is found that the upper rotor shows a decrease in the figure of merit as the separation distance approaches to zero. For the lower rotor, the figure of merit is much lower than that of the upper rotor, and it remains constant for most separation distance except near zero separation distance, in which it slightly increases. The iterative BEMT prediction captures the trend of the figure of merit for the upper rotor and lower rotor as a function of the separation distance. For the upper rotor, the prediction is in good agreement, but for the lower rotor, the prediction is overpredicted by about 10%. Both the measured and predicted figures of merit for the upper rotor converges to that for the isolated rotor for a large separation distance or Z/d greater than 0.5.

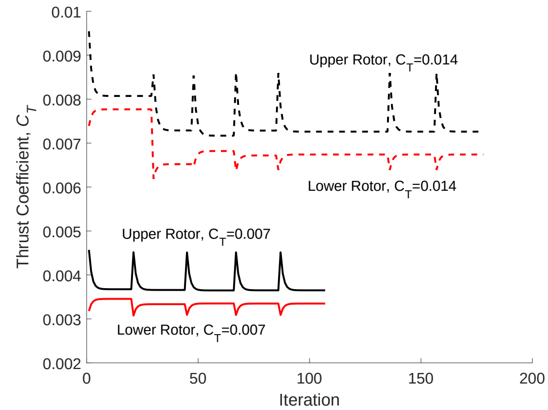

(a)

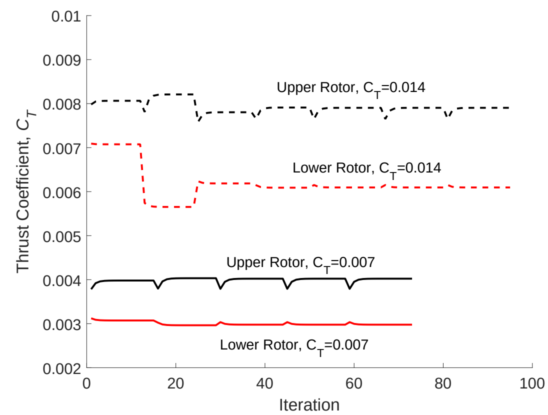

(b)

Fig. 8. Convergence history of Iterative BEMT and trim solutions: (a) Z/d=0.08 and (b) Z/d=1.0.

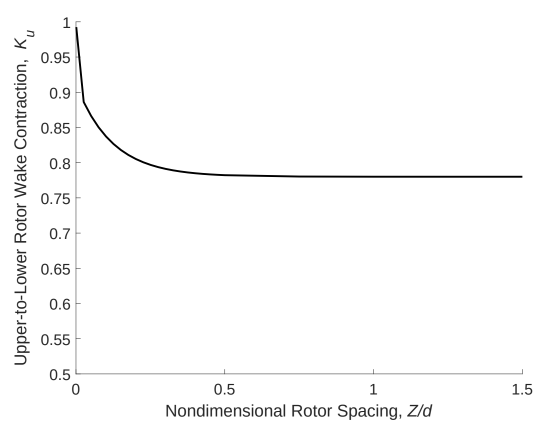

Fig. 9. Coaxial upper-to-lower rotor wake contraction as a function of the rotor spacing for $C_T = 0.014$.

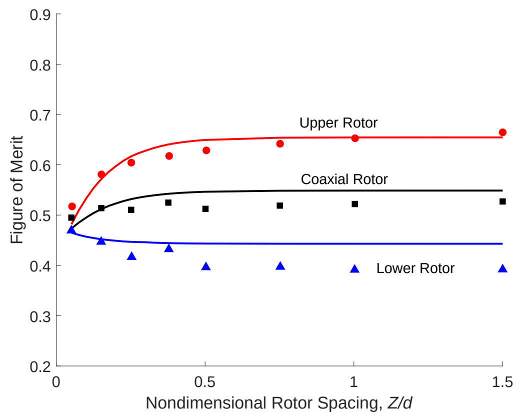

Fig. 10. Figure of merit as a function of the coaxial rotor spacing for $C_T = 0.014$.

Figure 11 shows the rotor thrust as a function of the rotor separation distance. For the separation distance larger than 0.5, the lower rotor carries only about 70% of the upper rotor thrust. As the separation distance decreases, the lower rotor thrust increases and approaches to 100% at near zero distance. The prediction shows about 10% higher thrust ratio for the lower rotor at large separation distance. Overall, however, the iterative BEMT predicts this thrust ratio trend accurately.

Figure 12 shows the power coefficients as a function of the rotor separation distance. It is shown that the profile powers remain constant for both rotors over the entire axial distance range. However, the induced powers increase as the rotor separation distance decreases since the rotor-to-rotor interference increases. The total power is the same for the upper rotor and the lower rotor due to the imposed torque-balanced trim condition.

Figure 13 shows the collective pitch angles for the upper and lower rotors as a function of the separation distance. It is shown that the lower rotor needs about an one degree higher collective pitch angle than the upper rotor beyond Z/d greater than 0.5 to meet the trim condition. This is attributed to the fact that the lower rotor experiences the higher induced velocity due to the influence of the upper rotor wake. As the separation distance decreases, two collective pitch angles increase and reach the same value in order to compensate the loss of the thrust due to higher induced velocities on the both rotors at a short separation distance.

Figure 14 shows two coaxial rotor loss factors. The first loss is referred to as the separation loss factor, which is denoted as κ_{sep}. This loss is the ratio of the coaxial rotor induced power to the single rotor induced power with the same solidity as the coaxial rotor for the same thrust, or a single rotor with six blades in this example: $\kappa_{sep} = \frac{P_{i,coax}}{P_{i,single,N_b=6}}$. As can be seen in Fig. 14 (a), this loss factor is less than 1.0 or the coaxial rotor is more efficient than the single rotor with the same solidity at large separation distance. Ramassamy (Ref. 9) attributed this higher performance of the coaxial rotor to the swirl recovery and the axial separation effects. However, also note that Bhagwat (Ref. 11) discussed that the swirl recovery is negligible in

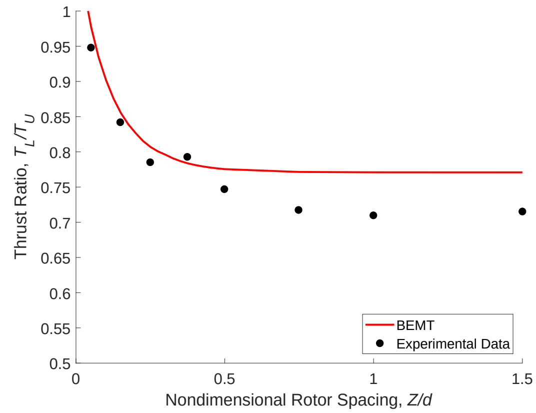

(a)

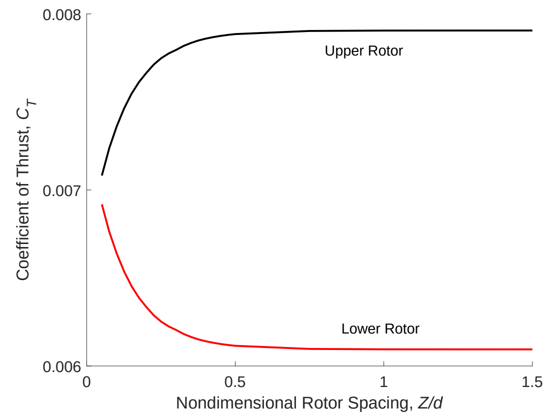

(b)

Fig. 11. Coaxial rotor thrust as a function of the rotor spacing for $C_T = 0.014$.: (a) thrust ratio and (b) thrust coefficient for the upper and lower rotors.

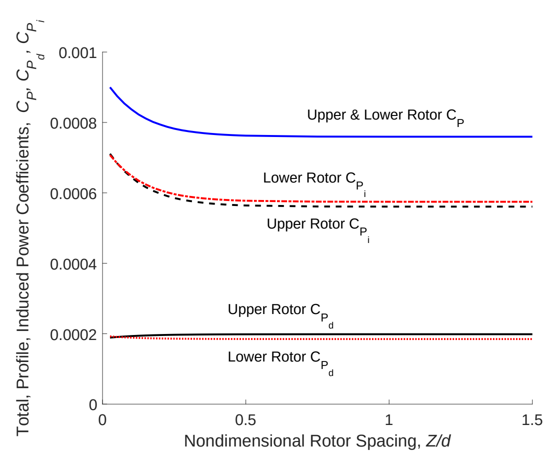

Fig. 12. Coaxial rotor power coefficient as a function of the rotor spacing for $C_T = 0.014$.

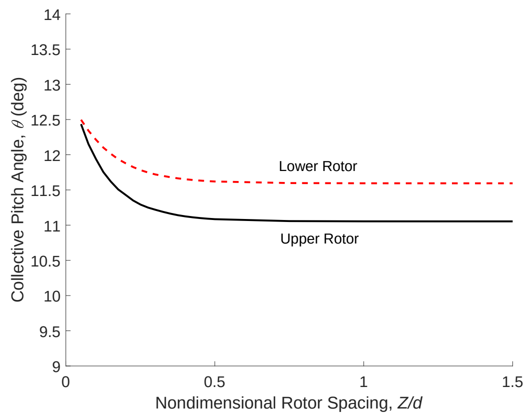

Fig. 13. Coaxial rotor collective pitch angle as a function of the rotor spacing for $C_T = 0.014$.

the coaxial performance gain. Leishman and Syal (Ref. 19) used a simple momentum theory to show that a six bladed rotor requires more power than two three-bladed coaxial rotors with the lower rotor operating in the fully contracted wake of the upper rotor. Our results are consistent with the earlier research. As the separation distance decreases, κ_{sep} approaches to one. At the rotor plane, this value should be exactly 1.0, but Fig. 14 (a) shows a slightly higher value than 1.0 in the rotor plane. This is because the rotor wake contractions are different for the single rotor, which is 0.707 in the far downstream, and for the coaxial rotor, which is 0.78 in the far downstream, as discussed. The interference loss, which is denoted as κ_{int}, is shown in Fig. 14 (b). This loss represents the increase in the coaxial rotor power with separation compared to two three-bladed rotors in one plane: $\kappa_{int} = \frac{P_{i,coax}}{2P_{i,single,N_b=3}}$. It is shown that 20-30% higher power is needed for a coaxial rotor. As the rotor distance decreases, the interference loss increases since the rotor-to-rotor effect increases. The prediction matches well with the measurement data.

Figure 15 shows the rotor-to-rotor interference factors as a function of the rotor separation distance. The upper or lower rotor power can be written as

$$P_{u|l} = P_d + P_i = P_o + \kappa\kappa_{u|l}\frac{T_{u|l}^{3/2}}{\sqrt{2\rho A}} \tag{25}$$

where $T_{u|l}$ denotes the thrust on the upper or lower rotor, κ represents the single rotor induced power loss factor and $\kappa_{u|l}$ represents the rotor-to-rotor interference factor for the upper or lower rotor. In other words, κ_u represents the induced power loss on the upper rotor due to the effect of the lower rotor and κ_l represents the induced power loss on the lower rotor due to the effect of the upper rotor. These loss factors can be obtained as

$$\kappa_{u|l} = K_{u|l}\frac{(C_{T_{req}}/2)^{3/2}}{(C_{T_{u|l}})^{3/2}} \tag{26}$$

where $C_{T_{req}}$ is the required total thrust and $K_{u|l}$ is given as

$$K_{u|l} = \frac{P_{i,u|l}}{P_{i,single}} \tag{27}$$

where $P_{i,u|l}$ is the induced power on the upper or lower rotor and $P_{i,single}$ is the induced power of a single rotor at $C_T = \frac{C_{Treq}}{2}$.

As can be seen in Fig. 15, both loss factors are greater than 1.0. The lower rotor influence loss factor is 60% higher than the upper rotor loss factor at a large axial separation distance. This indicates that the effect of the upper rotor on the lower rotor is much more significant than the opposite case or the lower rotor performs poor due to the wake of the upper rotor. As the axial distance decreases, the upper rotor influence factor rapidly increases or the upper rotor loses the performance as the effect of the lower rotor increases at short axial distances. This raised loss factor is also magnified with the reduced thrust on the upper rotor at short separation distances as shown in Fig 11 since the thrust coefficient appears in the denominator of Eq. (26). The lower rotor influence factor slightly decreases as the axial distance decreases. Even though the rotor induced velocity and the induced power increases on the lower rotor as the separation distance decreases, the thrust is also significantly increased as shown in Fig 11 to meet the desired overall coaxial rotor thrust requirement. This increase in the thrust results in slightly lowering the rotor-on-rotor influence factor on the lower rotor at short separation distances. Overall, the prediction captures the trend well for both the upper and lower rotors.

Figure 16 shows the local thrust, total inflow ratio, and angle of attack at three separation locations as a function of the non-dimensionaliezed radial location. At $Z/d = 0.08$ and 0.15, the upper rotor generates the higher thrust up to the non-dimensionalized radial position of about 0.8, but the lower rotor generates the higher thrust beyond this radial position. At $Z/d = 0.5$, the upper rotor generates the higher thrust over the entire blade radius than the lower rotor. The total inflow ratio shows that the lower rotor has a higher induced velocity than the upper rotor up to the non-dimensionalized radial position of 0.8, except $Z/d = 0.08$ in which the inflow ratios are almost identical for the two rotors at the outboard section. As the separation distance increases, the inflow ratio on the upper rotor is noticeably reduced on the entire blade section, but the inflow ratio on the lower rotor remains the same inside the upper rotor wake influence or contraction zone. Outside the upper rotor wake contraction zone, the inflow ratios of the lower rotor are shifted downward with increasing the separation distance. The upper rotor has no effect on this region. This transition location moves further toward the inboard as the separation distance increases because of the upper rotor wake contraction. Note that the angle of attack is greatly affected by the inflow and the collective pitch angle. For the outboard section ($r > 0.8$) at a short separation distance ($Z/d = 0.08$), the induced velocities are similar for the upper and lower rotors. As a result, the angle of attack of the lower rotor at the outboard ($r > 0.8$) is slightly higher than that of the upper rotor due to a higher collective pitch angle on the lower rotor, as shown in Fig. 13. With the exception of the outboard section, the upper rotor has higher angles of attack than the lower rotor due to a large inflow on the lower rotor, which results in the higher thrust for the upper rotor up to non-dimensionalized

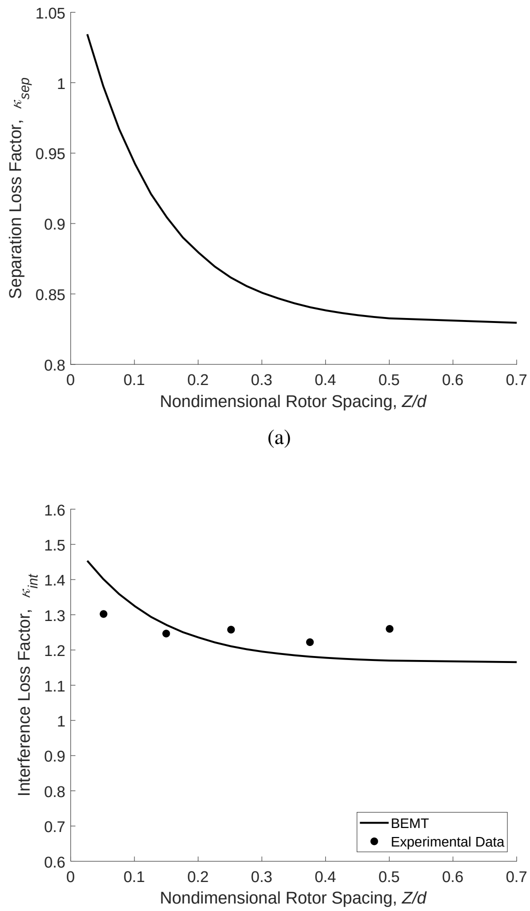

(a)

(b)

Fig. 14. Coaxial rotor loss factors as a function of the rotor spacing for $C_T = 0.014$.: (a) separation loss factor and (b) interference loss factor.

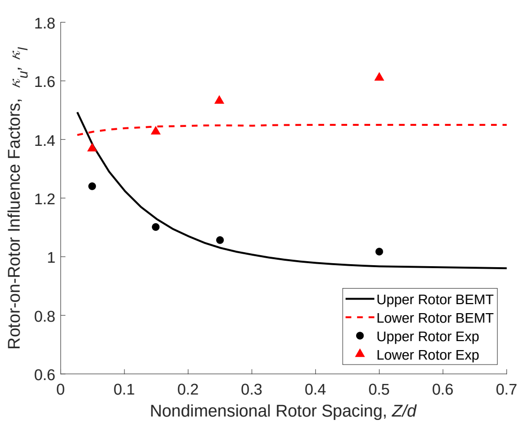

Fig. 15. Coaxial rotor-to-rotor influence factors as a function of the rotor spacing for $C_T = 0.014$.

radial position equal to 0.8 for $Z/d = 0.08$. At $Z/d = 0.5$, the lower rotor has the higher induced velocities or lower angles of attack or lower local thrusts compared to the upper rotor at the entire blade section.

Figure 17 shows the thrust ratio and the thrust coefficient for both the upper and lower rotors for the total coaxial rotor thrust coefficient of 0.007. Again, the BEMT prediction matches well with the measurement data for the thrust ratio. The lower thrust accounts for only around 70% of the upper rotor beyond $Z/d = 0.5$. Below $Z/d = 0.5$, the lower rotor thrust rapidly increases and approaches to the upper rotor thrust.

Figure 18 shows the power coefficients for the coaxial $C_T = 0.007$. The upper and lower rotor power coefficients are almost indistinguishable. The induced power increases as the separation distance decreases.

Figure 19 shows the local thrust coefficient, total inflow ratio, and angle of attack. The behaviors are similar to those for the higher C_T case. At $Z/d = 0.08$ and 0.15, the upper rotor generates higher thrust up to $r = 0.8$, and, beyond this position, the lower rotor generates higher thrust. At $Z/d = 0.5$, the upper rotor generates more thrust at the entire blade section. The total inflow ratio clearly visualizes the effect of the upper rotor wake contraction at different separation distances. The higher angles of attack and higher local thrusts are achieved on the lower rotor at the outboard section compared to the upper rotor at small separation distances.

CONCLUSIONS

An iterative BEMT model was developed to predict coaxial rotor performance and aerodynamics. In this method, the upper rotor solution is influenced by the lower rotor thrust and inflow and the lower rotor solution is affected by the upper rotor thrust and inflow. The mutual interaction is solved iteratively. Two empirical constants were added to match the measurement data.

The newly developed BEMT was validated against two coaxial rotor experiments. For Harrington's rotor, the thrust and power coefficients were well predicted for one specific axial separation distance. It was shown that the coaxial rotor performance is higher than each individual rotor at the same power. For Ramasamy's rotor experiment, the BEMT predicted the figure of merit, thrust, power, interference losses, etc. compared to the measurement data for two coaxial rotor C_T cases. It was found that the predictions are in good agreement with the data. The trends and magnitudes of the performance and loss were well captured in terms of the axial separation distance.

The detailed local aerodynamics were also predicted. It was found at relatively short separation distances, the upper rotor generates more thrust at the inboard and the lower rotor generates more thrust at the outboard. At large separation distances, the upper rotor generates more thrust at the entire blade section. The induced velocity and angle of attack supported this change of the trend.

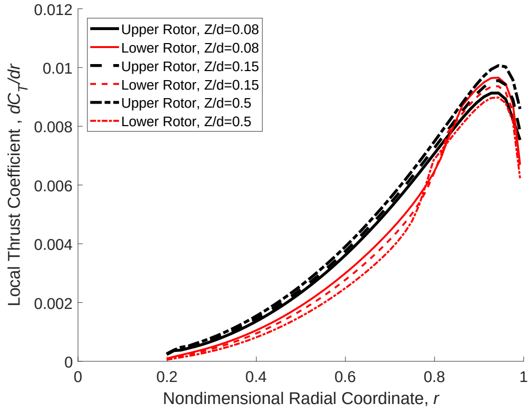

(a)

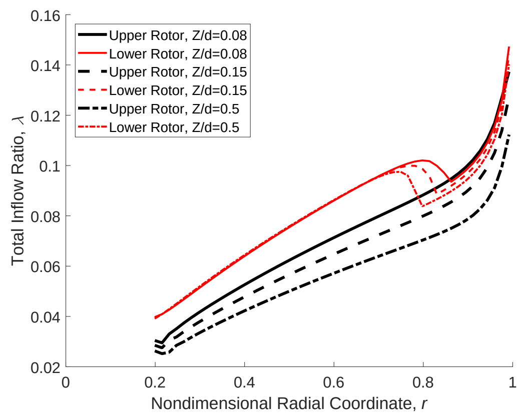

(b)

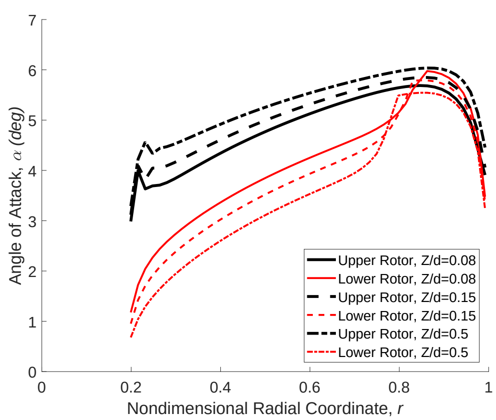

(c)

Fig. 16. Sectional aerodynamics for the upper and lower rotors at different spacing distances for $C_T = 0.014$.: (a) local thrust coefficient, (b) total inflow ratio, and (c) local angle of attack.

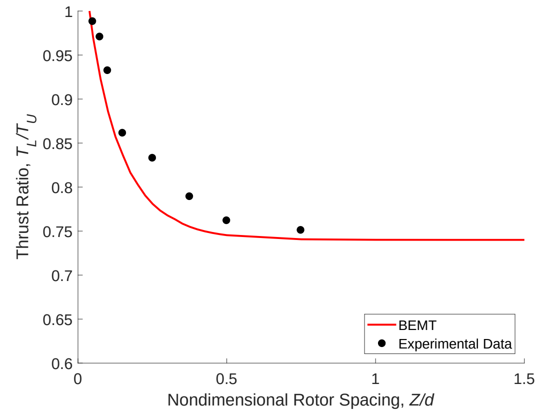

(a)

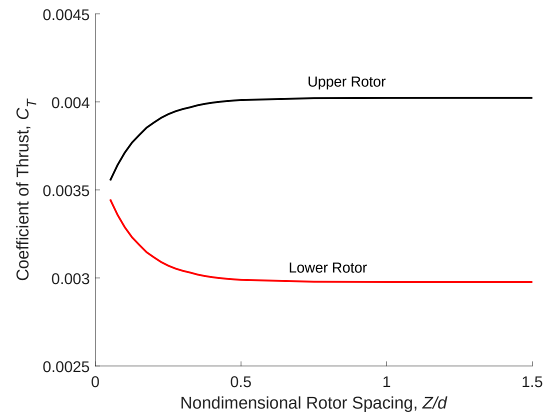

(b)

Fig. 17. Coaxial rotor thrust as a function of the rotor spacing for $C_T = 0.007$.: (a) thrust ratio and (b) thrust coefficient for the upper and lower rotors.

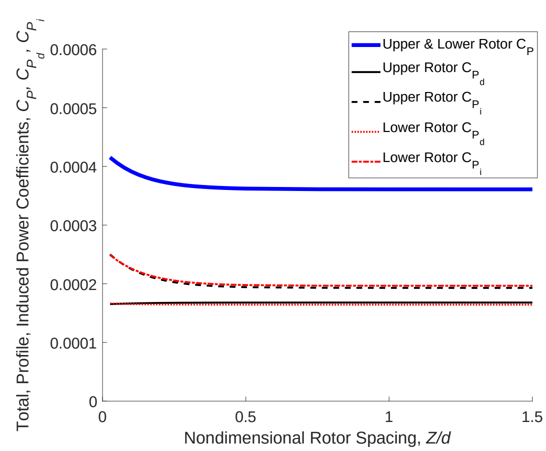

Fig. 18. Coaxial rotor power coefficient as a function of the rotor spacing for $C_T = 0.007$.

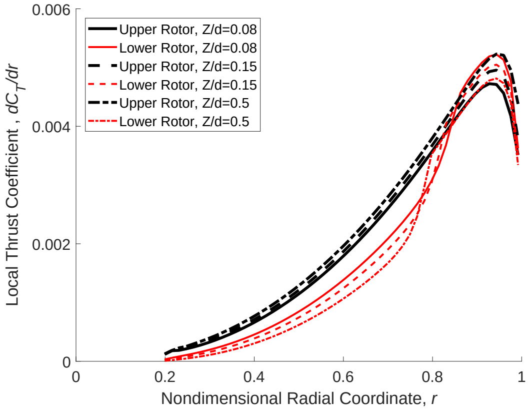

(a)

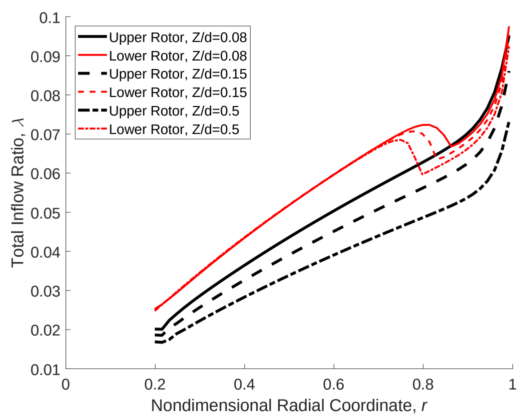

(b)

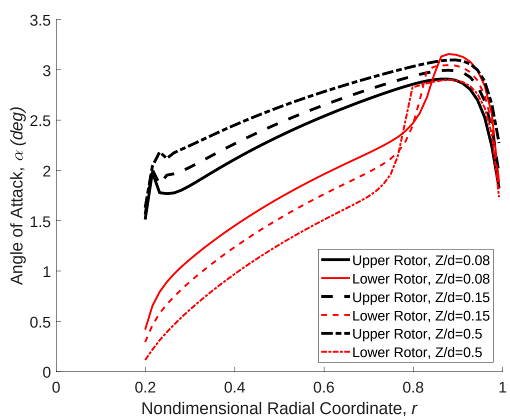

(c)

Fig. 19. Sectional aerodynamics for the upper and lower rotors at different spacing distances for $C_T = 0.007$.: (a) local thrust coefficient, (b) total inflow ratio, and (c) local angle of attack.

The newly developed BEMT code runs fast. It only takes a couple of minutes on a single desktop computer. This simple and fast computation allows for the preliminary design of a coaxial rotor. However, further validations are recommended to have a more confidence in this simple prediction method. For example, high-fidelity computational fluid dynamics (CFD) can be used to validate the BEMT results for local aerodynamic quantities.

REFERENCES

[1]Coleman, C. P., "A Survey of Theoretical and Experimental Coaxial Rotor Aerodynamic Research," NASA TP 3675, Washington, D.C., 1997.

[2]Cheney, M. C. J., "The ABC Helicopter," *Journal of the American Helicopter Society*, Vol. 14, 1969, pp. 1–10.

[3]Johnson, W., "Influence of Lift Offset on Rotorcraft Performance," NASA TP 2009-215404, Washington, D.C., 2009.

[4]Kim, H. W., Duraisamy, K., and Brown, R., "Aeroacoustics of a Coaxial Rotor in Level Flight," Ameican Helicopter Soceity 64th Annual Forum Proceedings, April 29–May 1 2008.

[5]Jacobellis, G., Gandhi, F., and Floros, M., "A Physics-Based Approach to Trim Optimization of Coaxial Helicopters in High-Speed Flight," Ameican Helicopter Soceity 71st Annual Forum Proceedings, May 5–7 2015.

[6]Herman, T. A., Celi, R., and Baeder, J. D., "Multidisciplinary Trim Analysis of a Coaxial-Pusher Rotorcraft Configuration," Ameican Helicopter Soceity 74th Annual Forum Proceedings, May 14–17 2018.

[7]Jia, Z., Lee, S., Sharma, K., and Brentner, K. S., "Aeroacoustic Analysis of a Lift-Offset Coaxial Rotor Using High-Fidelity CFD-CSD Loose Coupling Simulation," Ameican Helicopter Soceity 74th Annual Forum Proceedings, May 14–17 2018.

[8]Jia, Z., Lee, S., and Brentner, K. S., "Assessment of Turbulence Modeling and Wake-Grid Resolution for Lift-Offset Coaxial Rotor Simulations," 36th AIAA Applied Aerodynamics Conference, AIAA 2018-4120, June 25–29 2018.

[9]Ramasamy, M., "Hover Performance Measurements Toward Understanding Aerodynamic Interference in Coaxial, Tandem, and Tilt Rotors," *Journal of the American Helicopter Society*, Vol. 60, 2015, pp. 032005–1–032005–17.

[10]Ho, J. C., Yeo, H., and Bhagwat, M., "Validation of Rotorcraft Comprehensive Analysis Performance Predictions for Coaxial Rotors in Hover," *Journal of the American Helicopter Society*, Vol. 62, 2017, pp. 022005–1–022005–13.

[11]Bhagwat, "Co-rotating and Couter-rotating Coaxial Rotor Performacne," American Helicopter Society Aeromechanics Design for Transformative Vertical Flight, Jan 16–18 2018.

[12]Leishman, J. G., *Principles of Helicopter Aerodynamics,*, Cambridge University Press, New York, second edition, 2006.

[13]Payne, P. R., *Helicopter Dynamics and Aerodynamics*, The MacMillan Company, New York, NY, 1959.

[14]Leishman, J. G., "Aerodynamic Performance Considerations in the Design of a Coaxial Proprotor," *Journal of the American Helicopter Society*, Vol. 54, 2009, pp. 012005–1–022005–14.

[15]Giovanetti, E. B. and Hall, K. C., "Minimum Loss Load, Twist, and Chord Distributions for Coaxial Helicopters in Hover," *Journal of the American Helicopter Society*, Vol. 62, 2017, pp. 012001–1–012001–9.

[16]Landgrebe, A. J., "The Wake Geometry of a Hovering Rotor and Its Influence on Rotor Performance," *Journal of the American Helicopter Society*, Vol. 17, 1972, pp. 2–15.

[17]Harrington, R. D., "Full-Scale-Tunnel Investigation of the Static-Thrust Performance of a Coaxial Helicopter Rotor," Technical Report TN-2318, NACA, 1951.

[18]Lim, J. W., McAlister, K. W., and Johnson, W., "Hover Performance Correlation for Full-Scale and Model-Scale Coaxial Rotors," *Journal of the American Helicopter Society*, Vol. 54, 2009, pp. 032005–1–032005–14.

[19]Leishman, J. G. and Syal, M., "Figure of Merit Definition for Coaxial Rotors," *Journal of the American Helicopter Society*, Vol. 53, 2008, pp. 290–300.